Three-dimensional imaging and photostimulation by remote-focusing and holographic light patterning

Francesca Anselmi[a,1], Cathie Ventalon[a,1], Aurélien Bègue[a], David Ogden[b], and Valentina Emiliani[a,2]

[a]Wavefront-Engineering Microscopy Group, Neurophysiology and New Microscopies Laboratory, Centre National de la Recherche Scientifique UMR8154, Institut National de la Santé et de la Recherche Médicale U603, Université Paris Descartes, 45 Rue des Saints Pères, F-75006 Paris, France; and [b]Laboratoire de Physiologie Cérébrale, Centre National de la Recherche Scientifique UMR8118, Université Paris Descartes, 45 Rue des Saints Pères, F-75006 Paris, France

Edited by Erwin Neher, Max-Planck Institute for Biophysical Chemistry, Goettingen, Germany, and approved September 16, 2011 (received for review June 6, 2011)

Access to three-dimensional structures in the brain is fundamental to probe signal processing at multiple levels, from integration of synaptic inputs to network activity mapping. Here, we present an optical method for independent three-dimensional photoactivation and imaging by combination of digital holography with remote-focusing. We experimentally demonstrate compensation of spherical aberration for out-of-focus imaging in a range of at least 300 μm, as well as scanless imaging along oblique planes. We apply this method to perform functional imaging along tilted dendrites of hippocampal pyramidal neurons in brain slices, after photostimulation by multiple spots glutamate uncaging. By bringing extended portions of tilted dendrites simultaneously in-focus, we monitor the spatial extent of dendritic calcium signals, showing a shift from a widespread to a spatially confined response upon blockage of voltage-gated Na^+ channels.

Brain architecture, from the cellular up to the anatomical level, develops in three dimensions (3D): Dendritic and axonal trees often spread in extensive spatial patterns, organizing neuronal circuits into complex volumes. As an essential step in understanding how information is processed in the brain and studying the relationship between structure and function in cerebral circuits, techniques to stimulate and record neuronal signals in 3D are required. This need is particularly evident in research fields such as the study of dendritic integration and plasticity (1) or of neuronal network activity mapping (2, 3). Optical methods for stimulation and imaging enable targeting of a wide range of structures—from subcellular compartments up to multiple cells—within intact neuronal circuits, with millisecond and submicron resolution. Caged neurotransmitters and, more recently, optogenetic tools such as channelrhodopsin and halorhodopsin provide a diverse toolbox for neuronal excitation and inhibition (4, 5), whereas optical reporters such as calcium and voltage-sensitive dyes allow recording neuronal activity (6, 7).

Both imaging and photostimulation have been performed in 3D by using scanning or parallel excitation methods (8–12). However, to reach a full optical control of 3D structures, these approaches need to be combined into a unique optical system. One of the main challenges, in this respect, is to axially decouple the imaging and stimulation planes when both optical pathways are combined (as it is often the case) into the same microscope objective. Until now, simultaneous imaging and photostimulation have been limited to restricted areas, for example to the relatively short portion of a dendrite which extends in the focal plane of the microscope (13, 14), or, in the case of functional mapping, to neuronal bodies located on the same plane (15).

To overcome these limitations, we propose here a unique scanless optical system for simultaneous imaging and stimulation in 3D. Wide-field imaging on arbitrary oriented planes is achieved by using a remote-focusing technique adapted from Botcherby et al. (16). In its initial implementation, remote-focusing was proposed as a method for rapid 3D scanning. Here, we demonstrate that a similar scheme can be used to perform epifluorescence and functional imaging along arbitrary tilted planes at different axial locations. In addition, we combine the system with 3D single-photon holographic stimulation (12, 17), and apply this setup for fast photoactivation (through multiple spots glutamate uncaging) and high frame rate functional imaging of oblique dendritic segments in brain slices over a length of approximately 200 μm. We demonstrate recording of high resolution (micrometric) spatial information on dendritic signals by monitoring Ca^{2+} responses before and after block of voltage-gated Na^+ channels.

Results

Coupling Digital Holography with Remote-Focusing. The experimental microscope is schematized in Fig. 1. It includes light paths for digital holography (purple path), epifluorescence illumination (blue path), and remote-focusing (green path). Generation of 3D multiple diffraction-limited spots for photolysis at 405 nm (18) is achieved using a conventional digital holography arrangement (12, 17, 19) through the principal objective O1 (*SI Materials and Methods*). Axial scanning is performed at a remote location to image in 3D without modifying the position of the photoactivation spots. A perfect 3D image (*Img*) of the fluorescent object is reconstructed around the focal plane of a remote objective (O2). As detailed in the next section, the conditions for perfect 3D imaging depend only on the magnification of the telescope, which images the back pupil plane of O1 onto that of O2. An adjustable mirror (M_R) placed in the image space of O2 then creates a 3D mirror image (*Img'*) of the object, which is the symmetric of *Img* with respect to M_R (Fig. 1, *Insets*). By translating or tilting M_R, *Img'* can be moved to a different axial position or rotated around the x_2 and y_2 axes. Finally, a CCD camera images the intersection of *Img'* with the focal plane of O2. The section of the object that appears in-focus at the camera can therefore be chosen by tilting and/or axially displacing M_R. Note that fluorescence light coming from O1 is spatially separated from that reflected by M_R by a polarizing beam combiner (P) and a quarter-wavelength plate ($\lambda/4$) placed right before O2. This arrangement is more efficient by a factor of 2 than a 50/50 beam splitter in terms of fluorescence light collection (16) (*SI Materials and Methods*).

Characterization of Aberrations in the Remote-Focusing System. The theory underlying the formation of a 3D perfect image within the remote-focusing system was fully developed by Botcherby et al. (20) and is just briefly summarized here.

Author contributions: F.A., C.V., D.O., and V.E. designed research; F.A. and C.V. performed research; F.A., C.V., and A.B. analyzed data; A.B. contributed to conceive the proof of principle experiments in brain slices; and F.A., C.V., A.B., and V.E. wrote the paper.

The authors declare no conflict of interest.

This article is a PNAS Direct Submission.

[1]F.A. and C.V. contributed equally to this work.

[2]To whom correspondence should be addressed. E-mail: valentina.emiliani@parisdescartes.fr.

This article contains supporting information online at www.pnas.org/lookup/suppl/doi:10.1073/pnas.1109111108/-/DCSupplemental.

We consider a point source at position **r**(x,y,z) in the object space of a high N.A. microscope objective obeying the sine condition (20). In the linear regime, for small displacements of the point source from the focal point ($r \ll f$, where f is the focal length of the objective), the wavefront generated at the pupil of the objective can be written as (20):

$$\Psi(\rho,\phi,r) \approx -nk\{x\rho\sin\alpha\cos\phi + y\rho\sin\alpha\sin\phi + z\sqrt{1-\rho^2\sin^2\alpha}\}, \quad [1]$$

where ϕ is the azimuth angle and ρ the normalized radial distance in the pupil of the objective, k the wavenumber, and nsinα the N.A. of the objective. From Eq. **1**, we can infer that a displacement of the point source in the x-y plane corresponds to horizontal and/or vertical tilt of the wave front at the pupil. The z-dependent term, corresponding to an axial displacement of the point source, includes multiple components, the first due to defocus and the others to spherical aberrations, which deteriorate imaging outside the focal plane of the objective. The z-dependent optical aberrations become explicit if the z-term in Eq. **1** is developed in powers of ρ and further decomposed into the Zernike polynomial basis (21):

$$\Psi(\rho,\phi,z) = 2\pi\sum_{n=0}^{\infty}\sum_{m=-n}^{n} c_n^m(z)Z_n^m(\rho,\phi). \quad [2]$$

The Zernike coefficients for defocus, first-order, and second-order spherical aberrations resulting from this decomposition are specified in Table S1, together with the corresponding Zernike polynomials.

The odd parity of the pupil function in the linear regime (Eq. **1**) permits compensation of spherical aberrations introduced by the principal microscope with a second symmetrical microscope. The principle is to image the pupil of the principal objective (O1) into the pupil of a remote objective (O2) using a telescope (L1-L2) with a magnification chosen such that the effective angular semiaperture (sin α) is identical for both objectives. It can be shown that the required magnification for the telescope is (20) $\frac{f_{L2}}{f_{L1}} = \frac{n_2 f_{O2}}{n_1 f_{O1}}$ ($n_{1,2}$, refractive indices in the object and remote spaces). As a result, spherical aberrations introduced by O1 are compensated by the opposite amount of spherical aberrations introduced by O2, and a perfect image of the point source is created in the remote space at position $\mathbf{r_2} = -\mathbf{r_1}n_1/n_2$ ($\mathbf{r_{1,2}}$, coordinates in the object and remote spaces). For an extended object, this results in perfect imaging of the sample at all axial planes, within the limit of the linear regime (20).

To compensate for spherical aberrations in our system, we first measured the axial range in which the linear approximation of Eq. **1** was justified. We used a multilateral shearing interferometer [SID4-028, Phasics SA (22)] as a wave front analyzer, and measured z-dependent optical aberrations as a function of the axial position of a point source in a simple microscope. The experimental configuration is shown in Fig. 2*A*. A collimated laser beam (473 nm, Laser Quantum, Ciel Laser) was focalized by the microscope objective, thus creating a point source in the object space (*SI Text*). A mirror (M_O) was used to form a symmetrical image of this point: Axially translating M_O was then equivalent to displacing the point source of twice the distance. A telescope imaged the pupil plane of the objective into the plane of the wave front analyzer, where the spatial phase of the beam was measured

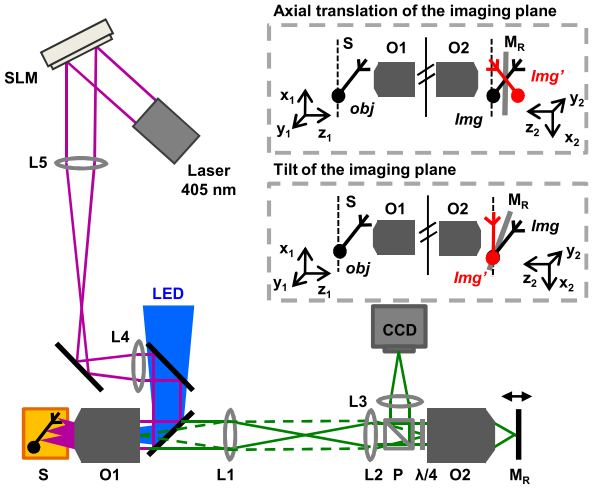

Fig. 1. Combined remote-focusing and digital holography setup. Purple path, digital holography. Blue path, epifluorescence. Green path, remote-focusing system generating a remote image of the sample (solid line), by imaging the pupil plane of O1 into that of O2 (dashed line). S, sample; O1, objective Olympus, water immersion, 40×, 0.8 N.A.; O2, objective Olympus, dry, 40×, 0.75 N.A.; L1-L5, achromatic lenses [focal lengths (millimeter), $f_{L1} = 200$; $f_{L2} = 150$; $f_{L3} = 150$; $f_{L4} = 300$; $f_{L5} = 500$]; P, polarizing beam combiner; $\lambda/4$, quarter wavelength plate; M_R, remote mirror; SLM, spatial light modulator. (*Insets*) Formation of the remote image (*Img*) and of the mirror image (*Img'*, red), following axial translation (*Top*) or tilting (*Bottom*) of M_R.

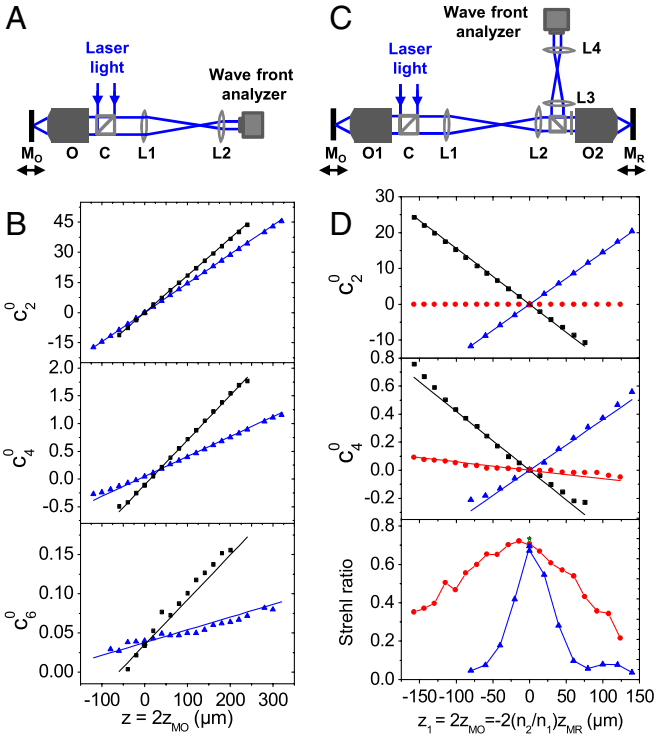

Fig. 2. Characterization of defocus and spherical aberrations in the remote-focusing setup. (*A*) Optical setup used for characterization of z-dependent aberrations introduced by a single objective (O1 or O2). M_O, mirror in object space; L1, L2 achromatic lenses [focal lengths (millimeter), $f_{L1} = 200$; $f_{L2} = 100$]; C, 50/50 beam splitter cube. (*B*) Zernike coefficients for (*Top* to *Bottom*) defocus (C_2^0), first-order (C_4^0), and second-order (C_6^0) spherical aberrations, measured with the setup of *A*, experimental data (blue triangles and black squares, for O1 and O2, respectively) were in agreement with theoretical predictions (blue and black lines, for O1 and O2, respectively) obtained in the linear approximation for $N.A._{O1} = 0.76$ and $N.A._{O2} = 0.72$. (*C*) Remote-focusing setup modified for aberration measurements. L1-L4, achromatic lenses [focal lengths (millimeter), $f_{L1} = 200$; $f_{L2-L3} = 150$; $f_{L4} = 100$]. (*D*, *Top* and *Middle*). Zernike coefficients for defocus (C_2^0) and first-order spherical aberration (C_4^0) introduced by O1 (blue triangles), O2 (black squares) were measured in the setup of *C* by moving M_O or M_R, respectively. Then, defocus was canceled (*Top*, red circles) by moving M_O and M_R simultaneously. First-order spherical aberration was almost perfectly compensated (*Middle*, red circles) and could be well approximated by summing (red line) the linear fits of first-order spherical aberrations introduced by O1 and O2 (blue and black lines, respectively), in agreement with theory. (*Bottom*) Measured Strehl ratio for uncompensated (blue triangles) and compensated (red circles) configurations. The green star corresponds to the Strehl ratio measured in setup *A* with objective O1 (without the remote-focusing unit).

for different positions of M_O. Experimental values of defocus, first-order, and second-order spherical aberrations (Fig. 2*B*) were obtained individually for the objectives O1 (blue triangles) and O2 (black squares) by decomposing the measured wave front on the Zernike polynomial basis. Linear dependence on axial displacement was observed in an interval of 400 μm. The experimental data could be fitted with the theoretical equations for the Zernike coefficients (Table S1), by using an N.A. slightly smaller than the nominal one (0.76 instead of 0.8 for O1, Fig. 2*B*, blue lines; 0.72 instead of 0.75 for O2, Fig. 2*B*, black lines). Theory and experiments showed that the major contribution to degradation of out-of-focus imaging is due to first-order spherical aberration, with just a minor participation of second-order spherical aberration.

We then measured the experimental range of spherical aberration compensation in the remote-focusing setup. We placed the wave front analyzer in a plane conjugated with the pupils of O2 and O1, as shown in Fig. 2*C*. In this setup, we measured again the defocus and first-order spherical aberration introduced by O1 and O2 by moving the mirror M_O (for O1), or the remote mirror M_R (for O2). The results are plotted in Fig. 2*D* (*Top* for defocus and *Middle* for first-order spherical aberration), as a function of $z_1 = 2z_{MO} = -2(n_2/n_1)z_{MR}$. For O1 (blue triangles), we obtained the same results as previously, which can be fitted assuming an angular aperture of $\sin\alpha_1 = \text{N.A.}_1/n_1 = 0.57$ (blue line). Because in this setup the effective angular aperture of O2 is reduced to match the angular aperture of O1 ($\sin\alpha_1 = \sin\alpha_2$), defocus and first-order spherical aberration introduced by O2 (black squares) are equal and opposite to those introduced by O1. Experimental data can be fitted assuming an angular aperture of $\sin\alpha_2 = 0.59$ (black line). The slight mismatch between the two effective angular apertures could be due to the objectives not perfectly obeying the sine condition or possibly to an imprecision on the focal lengths of L1 and L2.

Next, we displaced the two mirrors simultaneously, in such a way that the defocus introduced by O1 was canceled by the defocus introduced by O2 (Fig. 2*D*, *Top*, red circles). In this situation, the mirror M_O was positioned to give an out-of-focus point source, whereas the remote mirror M_R allowed refocusing. First-order spherical aberration was well-compensated within an axial range of 300 μm (Fig. 2*D*, *Middle*, red circles). The residual spherical aberration was compatible with the slight mismatch in the effective angular apertures of O1 and O2, and could be approximated by summing the spherical aberrations introduced by O1 and O2 (red line). Nevertheless, it remained in the range of the alignment precision (i.e., comparable with other measured aberrations, Fig. S1).

To estimate the improvement of the overall imaging quality due to compensation of spherical aberrations in the remote-focusing setup, we computed the Strehl ratio from the measured wave fronts. This parameter is an evaluation of the imaging performance; it corresponds to the ratio between the maximal intensities of the point spread functions in an experimental system and in a perfect imaging system (21). The Strehl ratio for different z values (Fig. 2*D*, *Lower*) was obtained by axially displacing M_O alone (blue triangles), or by displacing M_O and M_R simultaneously (red circles). The first situation would correspond to refocusing by displacing the camera, whereas the second situation corresponds to aberration-free refocusing with the remote mirror. A large improvement of the Strehl ratio was observed in the latter case. The Strehl ratio never reached the optimal value of 1 (perfect imaging system), even when the two mirrors were in-focus (maximum value of 0.72). However, the corresponding aberrations did not originate from the remote-focusing unit, but were already present in the principal microscope (green star, Strehl ratio of 0.73).

Imaging Along a Tilted Plane. The ability to create a 3D aberration-free replica of the object also allows imaging along an oblique plane by tilting the remote mirror M_R with respect to the optical axis, around x_2 and/or y_2 (Fig. 1, *Inset*). The maximum tilt is limited both by mechanical and optical constraints.

Mechanically, the maximum angle is obtained when the mirror surface hits the objective. Here, we used a one-inch mirror (M_R) and an objective (O2) of working distance WD = 0.51 mm and of outer diameter $d = 8.5$ mm (on the mirror side). This implementation allows for a maximum angle of the mirror equal to 7° ($\approx \arctan\frac{2\text{WD}}{d}$), leading to a maximum tilt of the remote image (*Img'*) twice larger, 14°. Because the magnification between the remote image and the object is identical in the three dimensions (equal to n_1/n_2), this configuration is equivalent to tilting the object of the same angle.

Optically, the main limitation comes from clipping of the light beam reflected by M_R. Indeed, when M_R is tilted, the reflected beam at the pupil of O2 is laterally displaced (Fig. 3*A*). For small angles, this displacement should introduce no aberrations on the output beam. However, for angles larger than the difference between the full and the effective angular semiapertures of O2 ($\sin\beta = \text{N.A.}_{O2}/n_2$ and $\sin\alpha_2 \approx \text{N.A.}_{O1}/n_1$, respectively), a portion of the reflected beam is clipped at the back pupil of O2, leading to a loss in resolution. Here, we estimated that $\beta = 46°$ and $\alpha_2 = 36°$ (from $\text{N.A.}_{O2} = 0.72$ and $\sin\alpha_2 = 0.59$), giving a maximal tilt of the remote image (and thus a maximal equivalent tilt in the object space) before clipping of 10°. Yet, in our conditions, the loss in resolution was negligible and the imaging quality (Strehl ratio) was not significantly affected by tilting M_R in the full range allowed by mechanical constraints (±14°, Fig. 3*B*).

As recently shown by Smith et al. (23, 24), another cause of loss in lateral resolution when imaging along an oblique plane is due to the tilt of the detection point spread function (PSF) compared

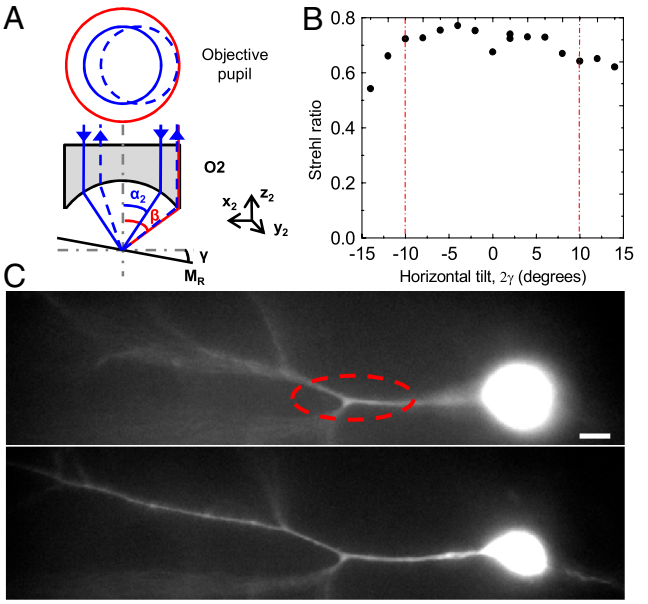

Fig. 3. Imaging along a titled plane. (*A*) Schematic of the incoming (solid blue line) and reflected (dotted blue line) beam at O2, with tilted M_R (*Bottom*, side view; *Top*, pupil plane): α_2, semiaperture angle of the incoming beam; β, semiaperture angle of O2; γ, M_R tilt angle with respect to the focal plane of O2 (corresponding to a tilt of the remote image twice larger). If γ exceeds the value of $(\beta\text{-}\alpha_2)/2$, part of the reflected beam is clipped by the pupil of O2, leading to resolution loss. (*B*) Strehl ratio measured for different values of 2γ (tilt of the remote image) with respect to the horizontal-axis (x_2). The setup was arranged as in Fig. 2*C*, but with $f_{L4} = 50$ mm. (*C*) CA1 pyramidal neuron filled with OGB-1, imaged before (*Top*) and after (*Bottom*) tilting M_R to compensate for the inclination of the apical dendrite to the surface of the slice (10°). Before tilting the mirror, only a small portion of the apical dendrite was in-focus (dashed red line), whereas the whole extent of the dendrite in the field-of-view (~200 μm) was in-focus after tilting. Scale bar, 10 μm.

to the original PSF, of twice the remote mirror angle. Therefore, the effective lateral resolution is a mixture of the lateral and axial sizes of the original PSF. However, for the low angles considered here, this effect is negligible.

To demonstrate imaging along an oblique plane in a biological preparation, we filled hippocampal CA1 pyramidal neurons with the fluorescence Ca^{2+} indicator Oregon Green Bapta-1 (OGB-1) through a patch pipette. After loading, the pipette was removed and the preparation transported to the remote-focusing setup. Images of the apical dendrite of a CA1 pyramidal neuron were obtained before and after tilting M_R by 5° (Fig. 3*C*). The tilt of the dendrite in the slice (10°) was previously estimated by performing a quick *z*-scan through the preparation with a piezoelectric element associated to O2. Tilting the image plane allowed following the whole length of the apical dendrite inside the field of view (200×150 μm), whereas only a small portion of dendrite was in-focus with an imaging plane perpendicular to the optical axis (dashed red line). Similar results were also obtained for layer V pyramidal neurons in neocortex (Fig. S2).

Three-Dimensional Glutamate Photolysis and Functional Imaging Along Tilted Dendrites. A major application of the method will be in functional imaging of neuronal processes. We performed 3D multiple spot photolysis of 4-methoxy-7-nitroindolinyl (MNI)-glutamate along dendrites of CA1 pyramidal neurons in the hippocampus, and recorded the Ca^{2+} signals evoked along tilted planes chosen to follow dendritic morphology. These neurons are excited by glutamate acting mainly at synaptic receptors of the AMPA and NMDA subtypes. NMDA receptors permit Ca^{2+} influx directly. Furthermore, cation influx through glutamate receptors evokes regenerative membrane potential changes dependent on voltage-gated Na^+ channels, and this depolarization activates voltage-gated Ca^{2+} channels. Thus, photoreleased glutamate will generate a rise of intracellular Ca^{2+} ion concentration that can be detected optically with fluorescent indicators. Here, MNI-glutamate (2 mM) was equilibrated into the bath with mixing at the beginning of the experiment. Neurons were filled with OGB-1 (100 μM) by whole cell patch-clamp. The pipette was removed after 20 min, before recording Ca^{2+} signals.

A first set of experiments consisted in photolysing caged glutamate at three locations (Fig. 4*A*, red arrows) on the tilted principal dendrite, and recording the evoked Ca^{2+} responses along that same dendrite. An example is shown in Fig. 4 *B–E*. Images of the principal dendrite of a pyramidal neuron, tilted by 12° with respect to the surface of the slice, were taken before (Fig. 4*B*) and after (Fig. 4*C*) tilting the imaging plane with the remote mirror. In this latter configuration, the dendrite could be observed over a length of approximately 170 μm. Variations of the fluorescence signal (10 Hz, 100 ms exposure time) were recorded after the uncaging event (2 ms pulse, total power 4.8 mW) (Fig. 4*D*, Movie S1), and measured over time with high spatial precision (<μm) and signal to noise ratio in the whole field of view. With these conditions of excitation, Ca^{2+} signals spread along the entire visible length of the principal dendrite and the cell body. The corresponding $\Delta F/F$ traces (single trial, Fig. 4*E*, *Left*) were calculated for regions of interest (ROIs) chosen along the apical dendrite (Fig. 4*C*, cyan). The same experiment was then repeated at a higher acquisition speed, by binning pixels on the camera. Ca^{2+} traces were acquired at 60 Hz (single trial, exposure time 15 ms, binning 4×4) for the same neuron (Fig. 4*E*, *Right*, Movie S2). In another neuron, by restricting imaging to a smaller region of the camera chip (200×17 μm), we were able to record the signal at 100 Hz (exposure time, 2 ms) (Fig. S3, Movie S3). Faster imaging was prevented by the acquisition speed of our CCD camera. Spatially extended Ca^{2+} responses similar to those shown in Fig. 4 *D* and *E* were observed in the majority of recorded neurons after simultaneous glutamate photolysis at three locations (8/10 tested neurons, 1–2 ms uncaging pulse, 4–6.5 mW).

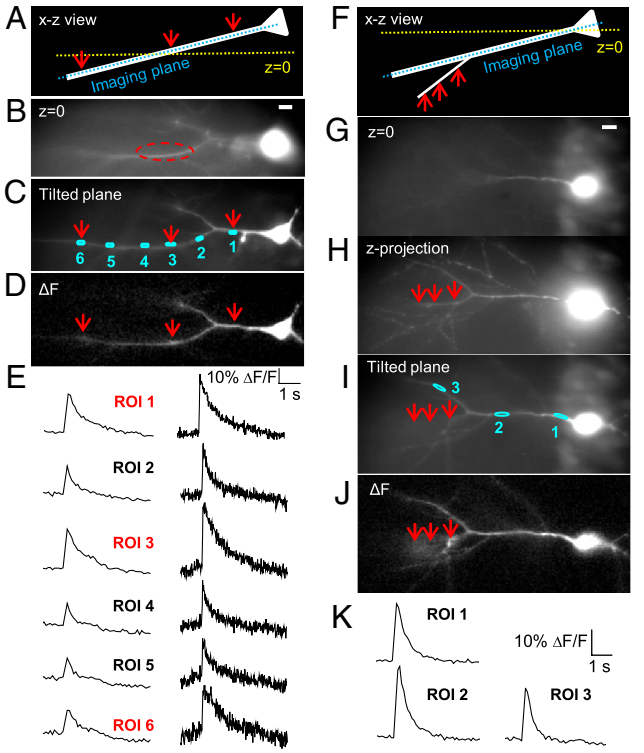

Fig. 4. Independent 3D photostimulation and Ca^{2+} imaging along a tilted plane in CA1 pyramidal neurons filled with OGB-1. (*A*) Schematic of the uncaging configuration corresponding to *B–E*: MNI-glutamate photolysis was performed at three locations along the tilted apical dendrite (red arrows, $z = -10.5$; 0, 7.5 μm for the proximal, medial and distal uncaging locations, respectively). (*B* and *C*) Images of the neuron before and after tilting the remote mirror to follow the direction of the principal dendrite in the brain slice (12°). (*D*) Ca^{2+} response (ΔF) measured 100 ms after photoactivation. The full time course is available as Movie S1. (*E*) Ca^{2+} responses ($\Delta F/F$) measured for different ROIs along the dendrite (1–8, cyan lines) at 10 Hz (*Left*) and 60 Hz (*Right*) acquisition rate. The ΔF movie at 60 Hz is available as Movie S2. (*F*) Schematic of the uncaging configuration corresponding to panels *G–K*: MNI-glutamate photolysis is performed at three locations on a thin branch off the apical dendrite (red arrows; $z = 18$, 22.5, 34.5 μm). (*G*) Fluorescence image of the neuron schematized in *F*, at the focal plane ($z = 0$). (*H*) Maximum intensity projection obtained from a *z*-stack of the neuron (40 frames; $\Delta z = 1.5$ μm), indicating the position of the uncaging spots, which are axially displaced with respect to the tilted imaging plane (full stack available as Movie S4). (*I*) Image of the neuron after tilting the imaging plane by 11° with the remote mirror. (*J*) Ca^{2+} response (ΔF) measured 100 ms after photolysis. The full time course movie is available as Movie S5. (*K*) Ca^{2+} responses ($\Delta F/F$) measured from three ROIs along the apical dendrite (*I*, 1–3 cyan lines) at 10 Hz. Scale bars, 10 μm.

To demonstrate that our system allows placing uncaging spots in 3D independently of the imaging plane, we performed glutamate uncaging on a secondary oblique dendrite, while recording Ca^{2+} signals from the principal one. An example is shown in Fig. 4 *F–K*. A *z*-scan (Fig. 4 *G* and *H*, Movie S4) was performed with the remote unit, to measure the inclination of the principal dendrite and to place the uncaging spots (red arrows) along a secondary dendrite. The imaging plane was tilted by 11° with the remote mirror to follow the inclination of the principal dendrite (Fig. 4*I*), leaving the secondary dendrite (and the uncaging spots) out-of-focus. Ca^{2+} responses were recorded following light stimulation (1 ms photolysis pulse, 4.9 mW): The ΔF images are shown in Fig. 4*J* and Movie S5. A small out-of-focus signal was observed in the region corresponding to the excited secondary branch, which spreads in the full visible portion of the in-focus principal dendrite. $\Delta F/F$ traces (Fig. 4*K*), shown here for three ROIs along the principal dendrite (Fig. 4*I*, cyan), had similar amplitude as those recorded in experiments where we directly stimulated

the principal dendrite (e.g., Fig. 4*E*). Similar experiments were repeated in three more neurons. A Ca^{2+} response was always observed in the out-of-focus secondary branch stimulated by photolysis ($N = 4$), but it only rarely extended to the apical dendrite (2/6 trials in $N = 2$ neurons).

To measure the electrical output at the soma that corresponded to Ca^{2+} signals spread over the whole principal dendrite, we performed control experiments in a conventional electrophysiological setup equipped with digital holography, in the same conditions as Fig. 4 *A–E* (three excitation locations on the apical dendrite, 4.8 mW). A single action potential or an action potential train was associated with Ca^{2+} responses spreading along the principal dendrite after glutamate uncaging (Fig. S4), suggesting that voltage-activated somatic and dendritic conductances contributed to generate the large Ca^{2+} signals in CA1 pyramidal cells (25–27). This hypothesis was tested by blocking voltage-gated Na^{+} channels with 0.5 μM TTX to reduce excitability. Ca^{2+} signals (ΔF, Fig. 5*A*) were recorded for a CA1 pyramidal neuron following photolysis of MNI-glutamate (uncaging at three locations on the apical dendrite, red arrows), before and after adding TTX to the bath: Drug application resulted in a shift from a widespread to a local Ca^{2+} signal, for the same stimulation conditions (two and four trials in the absence and presence of TTX, respectively; 1 ms pulse, 4.7 mW). Pooled data were obtained by stimulating two different groups of CA1 pyramidal neurons (1 ms pulse, 4–5.9 mW), either in control or in the presence of TTX. To estimate the spreading of Ca^{2+} response in the two conditions, we plotted $\Delta F/F$ signals (Fig. 5*B*) taken along segments of the dendrite (black lines, cartoon *Insets*) centered at the medial (*Top*) and distal (*Bottom*) uncaging positions in the absence (black) and presence (red) of TTX (distance from dendritic onset, mean ± SD, 65 ± 16 μm and 115 ± 23 μm); data for the proximal location were more difficult to interpret in the control conditions because of the vicinity of the soma. For each cell, $\Delta F/F$ was calculated as the average response in an interval of 100 to 400 ms after the photolysis pulse. The $\Delta F/F$ signals from different cells were normalized for the maximum and subsequently averaged; Ca^{2+} signal distribution was analyzed separately for the forward (i.e., toward the soma, Fig. 5*B*, *Right*) and backward (Fig. 5*B*, *Left*) directions. To ensure a comparison between similar responses in control and TTX experiments, only cells which presented a $\Delta F/F$ signal higher than 15% at the uncaging locations were considered in this analysis ($N = 4$ neurons for control and $N = 4$ neurons for TTX). In our experimental conditions, we observed that, above this threshold, control neurons always (4/4) developed a widespread response. At a distance of ±17 μm from the photolysis spot, $\Delta F/F$ was significantly smaller in the presence of TTX than in control conditions, for both forward and backward spreading, at the medial and distal locations (Fig. 5*C*). These results indicated that the spread of the Ca^{2+} signal depended on the excitability in perisomatic areas or in the first segment of the apical dendrite, involving the activation of voltage-gated Na^{+} conductances.

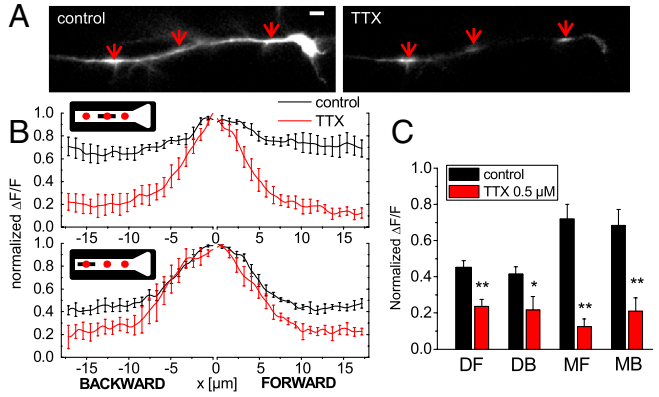

Fig. 5. Reduction in the spatial spread of dendritic Ca^{2+} signals by block of voltage-dependent Na^{+} channels. (*A*) In the same CA1 pyramidal neuron, Ca^{2+} responses (ΔF) measured 200 ms after photolysis of MNI-glutamate at three locations (red arrows), in the absence (*Left*) or presence (*Right*) of 0.5 μM TTX. The cell was filled with OGB-1. (*B*) Pooled data representing Ca^{2+} signals ($\Delta F/F$) averaged over different cells in the presence (red) or absence (black) of TTX. Thirty-five micrometers line profiles (*Insets*, black lines) were taken along the dendrite, centered on the medial (*Top*) and distal (*Bottom*) uncaging positions. Data are reported as mean ± SEM. Fluorescence signals ($\Delta F/F$) were normalized to its maximum for each cell before averaging. The average power was 4.7 mW, both in control (4.7 ± 0.9 mW) and in TTX (4.7 mW for all cells). (*C*) Histogram reporting mean ± SEM values of normalized $\Delta F/F$ at ±17 μm from the uncaging location. The level of Ca^{2+} signal was significantly smaller in the presence of TTX for the distal (D) and medial (M) uncaging locations, both in the forward (F) and in the backward (B) directions (DB, $N_{ctrl} = 3$, $N_{TTX} = 3$, $p = 0.04$; DF, $N_{ctrl} = 3$, $N_{TTX} = 4$, $p = 0.006$; MB, $N_{ctrl} = 4$, $N_{TTX} = 4$, $p = 0.003$; MF, $N_{ctrl} = 4$, $N_{TTX} = 4$, $p = 0.0003$). N values are identical for *B* and *C*. Laser pulse duration: 1 ms. Scale bar, 10 μm.

Discussion

We present an innovative combination of digital holography and remote-focusing, allowing for independent 3D imaging and photoactivation. This system provides a simple optical method to stimulate neuronal dendrites in 3D and record evoked responses in arbitrary planes, while preserving spatial information on signal distribution with high resolution (<μm).

An alternative possibility to image along oblique planes was recently presented by Dunsby (28), using a variant of the remote-focusing system described here. In this configuration a third microscope was built in the remote space and images on oblique planes were obtained by rotating the entire third microscope with respect to the optical axis. This implementation allows for a light efficiency twofold better than with our system, but is more complex than using a tilted remote mirror, and imposes a less favorable trade-off between the working distance of the remote objective and the amount of achievable tilt.

Decoupling of excitation and imaging could be obtained computationally instead of optically, by compensating the axial movement of the objective with a corrective phase imposed to the spatial light modulator (SLM), as demonstrated for optical tweezers (29). This method has the advantage of simplicity, as it can be readily implemented on any existing digital holography setup. However, it might not be compatible with fast axial scanning, because it is limited by the refreshing rate of the SLM and by the inertia of the scanning objective. Moreover it would not allow imaging on a tilted plane.

Alternative remote-focusing techniques have also been proposed. In general, any method which introduces a variable-focus lens into the fluorescent path would allow choosing the imaging plane independently of the excitation one (provided that spherical aberrations are compensated). For example, one such method consists in placing a deformable mirror in a plane conjugated to the pupil of the microscope objective (30). This technique is relatively simple and allows wide field out-of-focus imaging with correction of *z*-dependent aberrations at acquisition rates up to 200 Hz, but is not suitable for imaging along a tilted plane.

Functional imaging with high time resolution in a wide field configuration is currently used with calcium and voltage dyes to monitor signal propagation through dendritic and axonal trees (6, 7). Dynamics can be very fast, in the order of a few milliseconds (31), requiring high frame rates with submillisecond exposure times. However, until now, these studies were limited to dendritic branches lying in the focal plane. Tilting the imaging plane as described here gives access to a wider range of dendritic orientations, because long oblique branches can be brought into focus. With our CCD camera, we were limited to 100 Hz imaging rate (with 2 ms exposure time), but this performance would be improved severalfold with a more sensitive and faster camera. The remote tilting technique is a very general method that can

be applied to record, by functional imaging, responses evoked by electrode stimulation, photolysis or optogenetic photostimulation. We note that, even if our system was limited to a tilt angle of 14° by mechanical constraints, the use of a smaller remote mirror or a remote objective with a longer working distance would allow for a wider tilting range.

The combination of tilted imaging with digital holography permits a precise stimulation of specific points distributed in 3D throughout the dendritic tree, and makes our setup particularly useful to study phenomena of dendritic integration and compartmentalization, but also activity-dependent dendritic plasticity. Other potential applications, which do not specifically require oblique imaging, might take advantage of the capability of fast imaging in an aberration-free volume extending over hundreds of microns in 3D (Fig. 2*D*, Movie S4). In this respect, optogenetic compounds could be used to excite or inhibit a precise set of neurons in a circuit, while mapping network activity with calcium imaging by remote-focusing.

Finally, to increase penetration depth and axial resolution, one could perform both imaging and photoactivation in a two-photon configuration. Two-photon digital holography has been demonstrated for the generation of two-dimensional excitation light patterns (32–37) and could easily be implemented in 3D, with a holographic setup similar to the one presented in this work. The remote-focusing system described here can also be readily adapted to two-photon imaging, if the ultrafast excitation laser beam is coupled into the microscope through the remote-focusing unit (38, 39). The illumination beam can be scanned laterally with a pair of galvanometric mirrors, and axially by translating the remote mirror (40). An alternative implementation could take advantage of the idea presented in this manuscript of tilting the remote mirror, thus eliminating the need for axial scanning and simplifying the experimental setup.

Materials and Methods

Please, refer to *SI Materials and Methods* for detailed information.

Digital Holography. The phase of a 405-nm laser beam was modulated by a liquid crystal SLM. The SLM was imaged onto the back focal plane of objective O1 through a telescope and a low-pass dichroic beam splitter (Fig. 1, purple path). An iterative algorithm was used to compute the phase modulation in the SLM corresponding to the desired 3D distribution of diffraction-limited spots, as described in ref. 12.

Brain Slice Preparation. Transverse hippocampal slices were prepared from mice on postnatal days 16 to 30 in standard, ice-cold artificial cerebrospinal fluid. All experiments followed European Union and institutional guidelines of the care and use of laboratory animals (Council directive 86/609 European Economic Community).

Calcium Imaging and Glutamate Photolysis. Neurons were filled by whole cell patch-clamp with an intracellular solution containing 0.1 mM OGB-1. Extracellular solution was buffered with Hepes and contained bicarbonate to maintain intracellular pH. MNI-glutamate (2 mM) was equilibrated into the bath by mixing. After filling, the patch pipette was removed and the neurons were transferred to the digital holography/remote-focusing setup. Laser power was always measured after the principal objective.

ACKNOWLEDGMENTS. We thank E. Papagiakoumou, V. de Sars, M. Guillon for optimization of the 3D holographic algorithm, B. Amos, E. Botcherby, D. Débarre, J. Hayes, M. Oheim, P. Pedarzani, N. Ropert for fruitful discussions, K. Herault for mice caring, Phasics S.A. and Laser Quantum for helpful collaboration. F.A. was supported by the European doctoral school Frontières du Vivant and the Fondation pour la Recherche Médicale. A.B. was supported by Paris School of Neuroscience. D.O. was supported by the Centre National de la Recherche Scientifique and the Agence Nationale de la Recherche. D.O. and V.E. were supported by European Union Strep Photolysis (LSHM-CT-2007-037765). V.E. was supported by Human Frontier Science Program (RGP0013/2010) and Fondation pour la Recherche Médicale (FRM équipe).

1. London M, Hausser M (2005) Dendritic computation. *Annu Rev Neurosci* 28:503–532.
2. Haider B, McCormick DA (2009) Rapid neocortical dynamics: Cellular and network mechanisms. *Neuron* 62:171–189.
3. Arenkiel BR, Ehlers MD (2009) Molecular genetics and imaging technologies for circuit-based neuroanatomy. *Nature* 461:900–907.
4. Kramer RH, Fortin DL, Trauner D (2009) New photochemical tools for controlling neuronal activity. *Curr Opin Neurobiol* 19:544–552.
5. Gradinaru V, et al. (2010) Molecular and cellular approaches for diversifying and extending optogenetics. *Cell* 141:154–165.
6. Homma R, et al. (2009) Wide-field and two-photon imaging of brain activity with voltage- and calcium-sensitive dyes. *Philos Trans R Soc Lond B Biol Sci* 364:2453–2467.
7. Peterka DS, Takahashi H, Yuste R (2011) Imaging voltage in neurons. *Neuron* 69:9–21.
8. Vucinic D, Sejnowski TJ (2007) A compact multiphoton 3D imaging system for recording fast neuronal activity. *PLoS One* 2:e699.
9. Duemani Reddy G, Kelleher K, Fink R, Saggau P (2008) Three-dimensional random access multiphoton microscopy for functional imaging of neuronal activity. *Nat Neurosci* 11:713–720.
10. Kirkby PA, Srinivas Nadella KM, Silver RA (2010) A compact acousto-optic lens for 2D and 3D femtosecond based 2-photon microscopy. *Opt Express* 18:13720–13744.
11. Gobel W, Kampa BM, Helmchen F (2007) Imaging cellular network dynamics in three dimensions using fast 3D laser scanning. *Nat Methods* 4:73–79.
12. Yang S, et al. (2011) Three-dimensional holographic photostimulation of the dendritic arbor. *J Neural Eng* 8:046002.
13. Losonczy A, Magee JC (2006) Integrative properties of radial oblique dendrites in hippocampal CA1 pyramidal neurons. *Neuron* 50:291–307.
14. Kwon HB, Sabatini BL (2011) Glutamate induces de novo growth of functional spines in developing cortex. *Nature* 474:100–104.
15. Nikolenko V, Poskanzer KE, Yuste R (2007) Two-photon photostimulation and imaging of neural circuits. *Nat Methods* 4:943–950.
16. Botcherby EJ, Juskaitis R, Booth MJ, Wilson T (2007) Aberration-free optical refocusing in high numerical aperture microscopy. *Opt Lett* 32:2007–2009.
17. Lutz C, et al. (2008) Holographic photolysis of caged neurotransmitters. *Nat Methods* 5:821–827.
18. Trigo FF, Corrie JE, Ogden D (2009) Laser photolysis of caged compounds at 405 nm: Photochemical advantages, localization, phototoxicity, and methods for calibration. *J Neurosci Methods* 180:9–21.
19. Zahid M, et al. (2010) Holographic photolysis for multiple cell stimulation in mouse hippocampal slices. *PLoS One* 5:e9431.
20. Botcherby EJ, Juškaitis R, Booth MJ, Wilson T (2008) An optical technique for remote focusing in microscopy. *Opt Commun* 281:880–887.
21. Mahajan VN (2001) *Optical Imaging and Aberrations Part II. Wave Diffraction Optics* (SPIE, Bellingham, WA) p 97.
22. Velghe S, Primot J, Guerineau N, Cohen M, Wattellier B (2005) Wave-front reconstruction from multidirectional phase derivatives generated by multilateral shearing interferometers. *Opt Lett* 30:245–247.
23. Smith CW, Botcherby EJ, Booth MJ, Juskaitis R, Wilson T (2011) Agitation-free multiphoton microscopy of oblique planes. *Opt Lett* 36:663–665.
24. Smith CW, Botcherby EJ, Wilson T (2011) Resolution of oblique-plane images in sectioning microscopy. *Opt Express* 19:2662–2669.
25. Spruston N, Schiller Y, Stuart G, Sakmann B (1995) Activity-dependent action potential invasion and calcium influx into hippocampal CA1 dendrites. *Science* 268:297–300.
26. Golding NL, Spruston N (1998) Dendritic sodium spikes are variable triggers of axonal action potentials in hippocampal CA1 pyramidal neurons. *Neuron* 21:1189–1200.
27. Magee JC, Carruth M (1999) Dendritic voltage-gated ion channels regulate the action potential firing mode of hippocampal CA1 pyramidal neurons. *J Neurophysiol* 82:1895–1901.
28. Dunsby C (2008) Optically sectioned imaging by oblique plane microscopy. *Opt Express* 16:20306–20316.
29. Emiliani V, et al. (2005) Wave front engineering for microscopy of living cells. *Opt Express* 13:1395–1405.
30. Kner P, Sedat JW, Agard DA, Kam Z (2010) High-resolution wide-field microscopy with adaptive optics for spherical aberration correction and motionless focusing. *J Microsc* 237:136–147.
31. Canepari M, Djurisic M, Zecevic D (2007) Dendritic signals from rat hippocampal CA1 pyramidal neurons during coincident pre- and post-synaptic activity: A combined voltage- and calcium-imaging study. *J Physiol* 580:463–484.
32. Nikolenko V, et al. (2008) SLM microscopy: Scanless two-photon imaging and photostimulation with spatial light modulators. *Front Neural Circuits* 2:5.
33. Papagiakoumou E, de Sars V, Oron D, Emiliani V (2008) Patterned two-photon illumination by spatiotemporal shaping of ultrashort pulses. *Opt Express* 16:22039–22047.
34. Daria VR, Stricker C, Bowman R, Redman S, Bachor H-A (2009) Arbitrary multisite two-photon excitation in four dimensions. *Appl Phys Lett* 95:093701.
35. Papagiakoumou E, de Sars V, Emiliani V, Oron D (2009) Temporal focusing with spatially modulated excitation. *Opt Express* 17:5391–5401.
36. Antkowiak M, Torres-Mapa ML, Gunn-Moore F, Dholakia K (2010) Application of dynamic diffractive optics for enhanced femtosecond laser based cell transfection. *J Biophotonics* 3:696–705.
37. Dal Maschio M, et al. (2010) Simultaneous two-photon imaging and photo-stimulation with structured light illumination. *Opt Express* 18:18720–18731.
38. Salter PS, et al. (2009) Liquid crystal director dynamics imaged using two-photon fluorescence microscopy with remote focusing. *Phys Rev Lett* 103:257803.
39. Hoover EE, et al. (2010) Remote focusing for programmable multilayer differential multiphoton microscopy. *Biomed Opt Express* 2:113–122.
40. Botcherby EJ, Smith CW, Booth MJ, Juskaitis R, Wilson T (2010) Arbitrary-scan imaging for two-photon microscopy. *Proc SPIE* 7569:756917.